Carbon 125 (2017) 103–112

Contents lists available at ScienceDirect

Carbon

journal homepage: www.elsevier.com/locate/carbon

Tunable and weakly negative permittivity in carbon/silicon nitride composites with different carbonizing temperatures

Chuanbing Cheng [a, c, d], Runhua Fan [a, b, **], Zhongyang Wang [b, d], Qian Shao [e], Xingkui Guo [e], Peitao Xie [b, d], Yansheng Yin [a], Yuliang Zhang [a], Liqiong An [a], Yanhua Lei [a], Jong Eun Ryu [f], Akash Shankar [f], Zhanhu Guo [c, *]

[a] College of Ocean Science and Engineering, Shanghai Maritime University, Shanghai, 201306, PR China
[b] Dezhou Meta Research Center of Innovative Materials, Dezhou, 253000, PR China
[c] Integrated Composites Laboratory (ICL), Department of Chemical & Biomolecular Engineering, University of Tennessee, Knoxville, TN, 37996, USA
[d] Key Laboratory for Liquid-Solid Structural Evolution and Processing of Materials(Ministry of Education), Shandong University, Jinan, 250061, PR China
[e] College of Chemical and Environmental Engineering, Shandong University of Science and Technology, Qingdao, 266590, PR China
[f] Department of Mechanical Engineering, Indiana University-Purdue University Indianapolis, Indianapolis, IN, 46202, USA

ARTICLE INFO

Article history:
Received 3 July 2017
Received in revised form
30 August 2017
Accepted 10 September 2017
Available online 13 September 2017

Keywords:
Amorphous carbon
Metamaterial
Negative permittivity
Dielectric property
Silicon nitride

ABSTRACT

Despite the exotic electromagnetic properties have been demonstrated in metamaterials to date, how to effectively adjust negative electromagnetic parameters remains a challenge. Tunable negative permittivity is essential for the metamaterials to satisfy a variety of practical applications, such as capacitor, microwave absorbing and shielding. Here, we fabricated a random metamaterial, carbon/silicon nitride (C/Si_3N_4) composite, using a feasible impregnation-pyrolysis method. The microstructure and dielectric property of the composites with different heat treatment temperatures (HTTs) and carbon contents were investigated. The amorphous carbon membrane adhered on the rod-like Si_3N_4 grains. The negative permittivity behavior combined with inductive character was obtained in the composites, which was attributed to the low frequency plasmonic state generated from the formative conducting carbon networks. The magnitude of negative permittivity is demonstrated to be successfully adjusted by controlling the HTT and carbon content. The result is in good agreement with the analysis of Drude model. Interestingly, a weakly negative permittivity behavior was observed in the measured frequency, showing small negative values of permittivity between −50 and −10, which was ascribed to a moderate carrier concentration provided by the carbon networks. This work provides an effective way to achieve the tunable and weakly negative permittivity in random metamaterials.

1. Introduction

Electromagnetic metamaterials with negative permittivity or/and permeability have been the subject of intense research due to their unusual physical properties and exciting potential applications, such as negative refraction [1,2], optical imaging [3,4], electromagnetic cloaks [5–7], novel antenna [8,9] and sensor [10,11]. In the past few decades, although fascinating achievements of the metamaterials have been reported, great effort is still required to precisely control negative parameters as well as to achieve the desired functional properties [12,13]. Until now, two technical routes have been developed to prepare metamaterials: ordered metamaterials and random metamaterials [14]. Ordered metamaterials are artificially structured media with periodic unit cells, in which the negative parameters can be tuned by changing the design of the periodic structures, such as shape, size and geometric arrangement [15,16]. Whereas, the constructing process of the periodic structures is complex, and these metamaterials also show an anisotropic electromagnetic response, causing an adverse impact on the applications [17]. Random metamaterials without clear periodic array were proposed to overcome these limitations, which can be prepared using typical processing of material with ease [14,18]. Their electromagnetic properties can be feasibly tuned by tailoring the chemical compositions and microstructures, offering

* Corresponding author.
** Corresponding author. College of Ocean Science and Engineering, Shanghai Maritime University, Shanghai, 201306, PR China.
E-mail addresses: rhfan@shmtu.edu.cn (R. Fan), zguo10@utk.edu (Z. Guo).

http://dx.doi.org/10.1016/j.carbon.2017.09.037
0008-6223/

an efficient way to construct metamaterials with more freedom [19].

In the studying of random metamaterials, considerable attention has been paid to the development of metal composites to achieve tunable negative parameters. For instance, some metal particles (such as, Ni, Fe, Ag, Cu or Co) were randomly dispersed in insulating matrixs, and the tunable negative parameters were demonstrated in the obtained composites by tailoring their composition and microstructure [14,20–24]. Negative permittivity also was obtained in some metal alloy composites containing $Fe_{50}Ni_{50}$, FeNiMo or $Fe_{78}Si_9B_{13}$ particles [25–27]. Meanwhile, several recent studies were devoted to realize the negative permittivity in carbon composites with different carbon nanostructures, including graphene, carbon nanotube or nanofiber [18,19,28,29]. However, in those researches, there is little attention given to the magnitude of negative parameters, and negative value of permittivity is generally enormous. In fact, a weakly negative permittivity behavior with small negative value of permittivity in broad frequency range is desired for many applications. For example, the small negative magnitude of permittivity endowed a carbon based metamaterial with good impedance matching and improved absorption performance, benefiting its application in the microwave absorbing field [22,30]. High-permittivity was obtained in bilayer composites, which were constituted by the metamaterials with a suppressed negative permittivity, making them well apply in capacitors [31]. In addition, the weakly negative permittivity behavior can facilitate the applications of metamaterials in solar energy harvesting [7,32], sensor [33] and antennas [30].

Theoretical analysis indicates that the negative permittivity arises from the low frequency plasmonic state of free electrons in the random metamaterials, and the magnitude of negative permittivity closely associated with their free carrier concentration [14,23]. It is widely believed the low or moderate free carrier density is more beneficial to offer the weakly negative permittivity behavior in a wider frequency band [30,34,35]. Compared with the metals and nanostructured carbon materials, amorphous carbon materials with a relatively low carrier concentration can be regarded as a good candidate for constructing metamaterials, to attain the tunable and weakly negative permittivity behavior [36–38]. Besides, the amorphous carbon is easily synthesized from pyrolysis of organic precursors, and its electrical and microstructural properties can be tuned by controlling the heat treating condition, such as heat treatment temperature (HTT) [39].

Here we report the experimental realization of tunable negative permittivity behavior in amorphous carbon/silicon nitride (C/Si_3N_4) composites, which were prepared using a precursor impregnation and calcination process. Their magnitude of negative permittivity can be effectively controlled by adjusting the HTT and carbon content. The dielectric behavior was analyzed by the Drude model. Interesting, a weakly negative permittivity behavior with small negative value was also obtained in the testing frequency band (20 MHz-1 GHz).

2. Experimental

2.1. Sample preparation

The porous Si_3N_4 ceramics with the open porosity of ~50% were prepared by pressureless sintering under flowing nitrogen-gas, using the yttria (Y_2O_3) and ytterbia (Yb_2O_3) as sintering additives. The high-purity Si_3N_4 powders (α-Si_3N_4 > 93 wt%, particle median diameter < 0.5 μm; Beijing Tsinghua Unisplendor Founder High-Tech Ceramics Co. Ltd.), Y_2O_3 powders and Yb_2O_3 powders (the purity > 99.9%; Beijing Dk Nano technology Co. LTD. China) were used as starting materials. Firstly, the mixtures of Si_3N_4, 3 wt% Y_2O_3 and 6 wt% Yb_2O_3 powder were milled in ethanol for 48 h using the Si_3N_4 grinding media. After completely drying, the mixed powders were sieved with 100-mesh sieve and then cold isostatic pressed at 40 MPa. The green bodies were sintered at 1650 °C for 2 h in nitrogen atmosphere. Finally, the sintered ceramics were machined into square discs (15 mm × 15 mm × 2 mm) and then ultrasonically cleaned in ethanol.

For the preparation of C/Si_3N_4 composites, the obtained Si_3N_4 specimens were dipped into 1.5 g/ml or 1 g/ml sucrose aqueous solutions and vacuumized for 12 h to make the sucrose solution infiltrate into the Si_3N_4 discs. The specimens were then removed from the sucrose solution and dried in a ventilated oven at 80 °C for 12 h. After that, the as-received specimens were calcined at 500 °C for 1 h under flowing nitrogen-gas. After repeating impregnation-calcination process, the specimens with carbon content of 4.9, 8.3, 10.1, and 12.5 wt% were prepared. Finally, the as-prepared samples were calcined at 500, 850, 1100, and 1300 °C respectively, for 1 h in the nitrogen atmosphere to get the C/Si_3N_4 composites. For comparing and analyzing structural evolution, the carbon derived from sucrose powders was fabricated under the same calcination process.

2.2. Characterization

X-ray photoelectron spectroscopies (XPS) for chemical and compositional analysis were performed using an ESCALAB 250 photoelectron spectrometer (Thermo Fisher Scientific, USA). The phase structures of C/Si_3N_4 composites and pyrolysis carbon derived from sucrose carbonization were characterized by X-ray diffractometer (XRD, XD2/3, Beijing Purkinje General Instrument Co., Ltd., Beijng, China) with Cu Kα radiation. The diffraction patterns were collected in the diffraction angle ranging from 10 to 80° at room temperature in the air. The Raman spectra were recorded using a micro-Raman spectrometer (Jobin Yvon HR800, France) with 532.05 nm incident radiation. The microstructure of composites were observed using a field emission scanning electron microscope (FESEM, Hitachi SU-70, Tokyo, Japan), equipping with energy dispersive X-ray spectroscopy (EDX). Pore size distribution of the porous Si_3N_4 ceramic and its composites was characterized by the mercury porosimetry (Micromeritics Autopore IV 9500, Micromeritics, USA). The apparent porosity of the specimens was measured by the Archimedes' method. Agilent E4991A Precision Impedance Analyzer combined with 16453A dielectric test fixture was applied to determine the electrical properties of the composites. The impedance (Z', Z''), capacitance (C) and resistance (R_p) data at the frequency band from 20 MHz to 1 GHz were measured by the impedance analyzer under alternating current (ac) voltage (100 mV) at room temperature. The ac conductivity (σ_{ac}), the phase shift angle (φ), the real (ε') and imaginary (ε'') part of complex permittivity were calculated by the following formulas, respectively:

$$\sigma_{ac} = \frac{d}{RS} \tag{1}$$

$$\varphi = arctan\left(Z'' / Z'\right) \tag{2}$$

$$\varepsilon' = \frac{Cd}{\varepsilon_0 S} \tag{3}$$

$$\varepsilon'' = \frac{d}{2\pi f \varepsilon_0 S R_P} \quad (4)$$

where d is the specimen thickness, S is the electrode plate area, C is the capacitance, R_p is parallel resistance, R is real part of impedance ($R = Z'$), ε_0 is the permittivity of vacuum (8.85×10^{-12} F m^{-1}), and ω ($\omega = 2\pi f$) is the angular frequency.

3. Results and discussion

3.1. Composition and microstructure of the C/Si_3N_4 composites

X-ray photoelectron spectroscopy (XPS) characterizations were performed to analyze the composition and chemical states of composites at different HTTs, Fig. 1A. The clear C1s peak at ~285 eV verifies that carbon has been successfully hosted in porous Si_3N_4 matrix, and the Si2p, Si2s, N1s and O1s peaks also are observed at around 100, 150, 398 and 530 eV, respectively [40,41]. XPS C1s peak deconvolution of the composites is shown in Fig. S1A. Three peaks are utilized to fit the C1s region, with binding energies of 284.6 eV, 286.1 eV and 287.6 eV, corresponding to C═C/C–C, C–O–C and C═O groups, respectively [39]. Integrated areas of each extracted peak are computed to quantify the change in chemical composition of pyrolysis carbon, Fig. S1B. As the HTT increases, integrated area of peak corresponding to C–C/C═C group increases, which is suggestive of the structural transformation from C–O–C and C═O groups to C–C/C═C bonds. Meanwhile, a small amount of oxygen still retains in the pyrolysis carbon at high HTT.

Fig. 1B shows XRD patterns of C/Si_3N_4 composites with 12.5 wt% carbon content. The main diffraction peaks of the composites are β-Si_3N_4 and α-Si_3N_4 phases, and yet the characteristic peaks of pyrolysis carbon are indistinctive. This should result from that the carbon content is less, or the intensity of carbon peaks is much lower in comparison with those of other crystalline peaks. In order to explore the influence of HTT on crystallization of pyrolysis carbon, the sucrose powders were calcined under the same heat treatment process as that of composites, and their XRD patterns are given in Fig. S2. It is clear that carbon derived from pyrolysis of sucrose powder is amorphous, which have two broad characteristic peaks [(002) and (100)] in XRD patterns [42–44]. For the pyrolytic carbon at the HTT of 500 °C, the (100) peak is not obvious, while the graphite (002) peak appears at ~17°. As the HTT increases, the diffraction peaks become sharper and (002) peak shifts to a higher angle, identifying that the degree of ordered carbon structure increases [45–47].

Fig. 1C depicts the Raman spectra of the C/Si_3N_4 composites, and structural evolution of amorphous carbon with rising HTT is further revealed. Raman spectra are resolved into five peaks, namely, G (1590 cm^{-1}), D (1330 cm^{-1}), D′ (1620 cm^{-1}), D″ (1500 cm^{-1}) and I (1190 cm^{-1}) bands [48,49]. The G-band arises from the in-plane vibrations of the sp^2-bonded crystallite carbon [39]. The other peaks represent the structural defects and other disorder-induced effects for the carbon [50]. At the high HTT (1300 °C), the defect peaks are still intense, indicating the obtained pyrolysis carbon remains a highly disordered (turbostratic) form. I_D/I_G intensity ratio, which is calculated from the surface ratio of the D and G bands, can provide the microstructural information of carbon materials [39]. I_D/I_G ratio gradually decreases as the HTT increases from 850 to 1300 °C, which is attributed to the crystal growth and the higher graphitization degree. But the lower I_D/I_G ratio and weaker D peak are observed at 500 °C. The D band is usually ascribed to defects on the boundaries of the aromatic structures [45,51]. During the carbonization of sucrose, the depolymerization will lead to the formation of poly-aromatic structures [50]. At the HTT of 500 °C, the poly-aromatic unit boundary density is low, leading to the

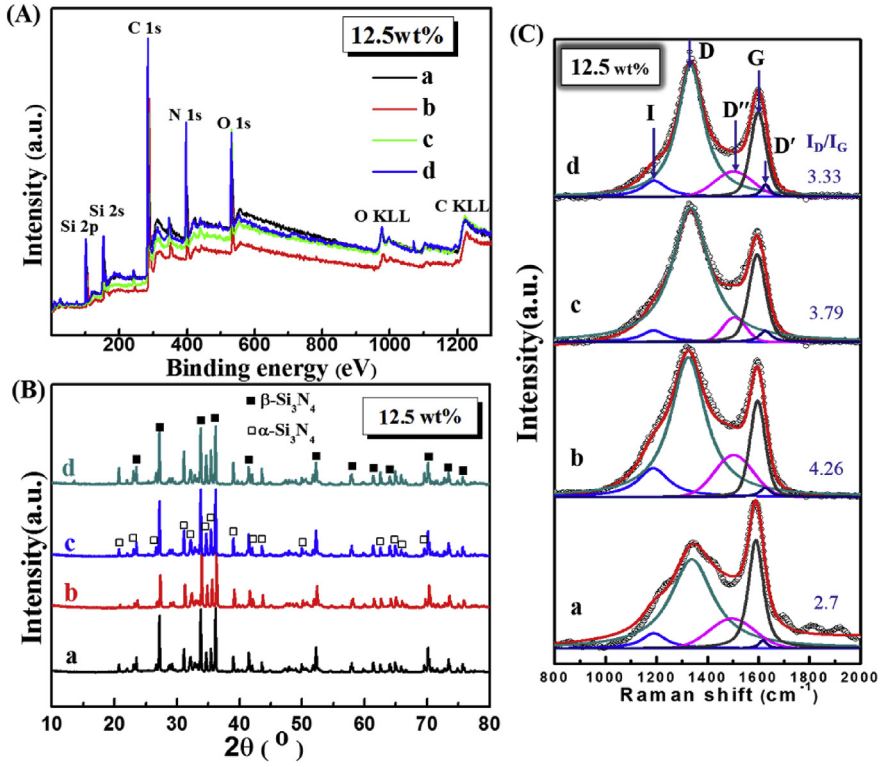

Fig. 1. XPS spectra (A), XRD patterns (B) and Raman spectra (C) of the C/Si_3N_4 composites with 12.5 wt% carbon content at the carbonizing temperature of (a) 500, (b) 850, (c) 1100 and (d) 1300 °C. (A colour version of this figure can be viewed online.)

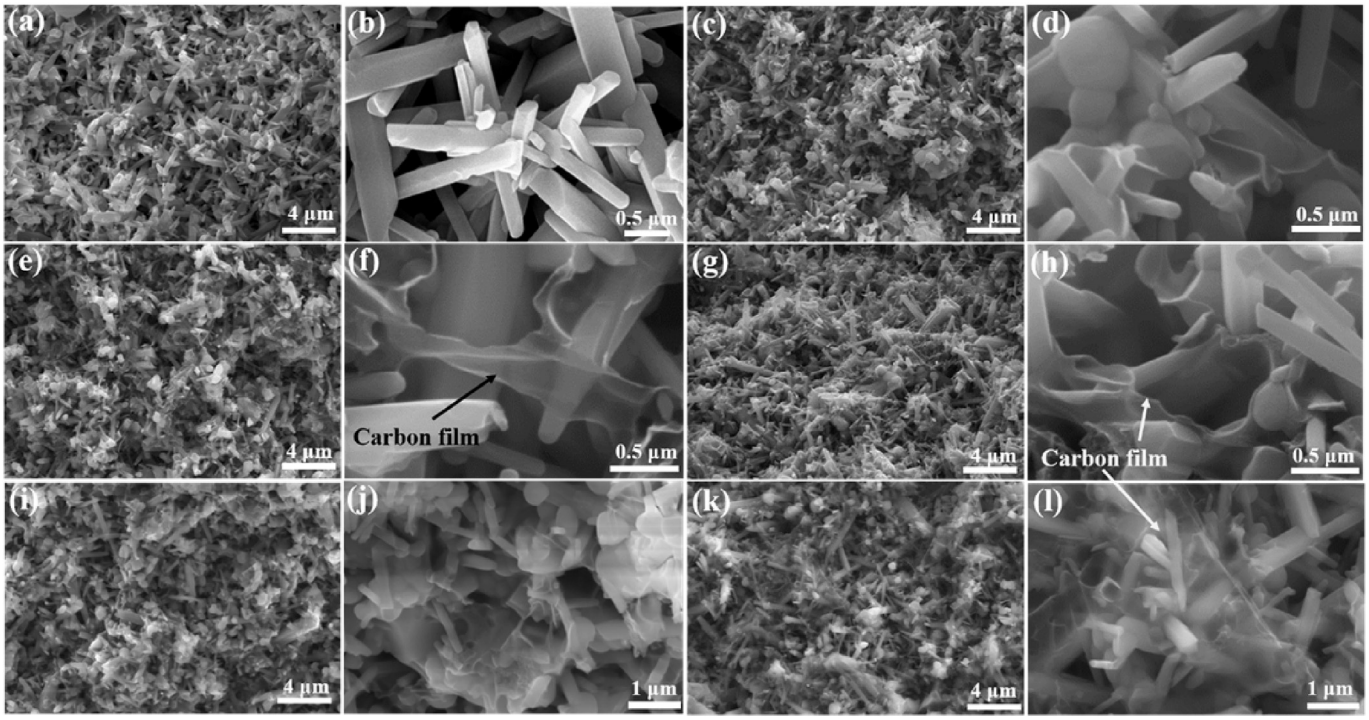

Fig. 2. FESEM images of the Si_3N_4 ceramic and its composites with different carbon contents and carbonizing temperatures. (a) and (b) porous Si_3N_4 ceramic; (c) and (d) 5 wt%, 1100 °C; (e) and (f) 8.3, 1100 °C; (g) and (h) 10.1 wt%, 1100 °C; (i) and (j) 12.5 wt%, 500 °C; (k) and (l) 12.5 wt%, 1300 °C.

decrease of D band intensity and I_D/I_G ratio. Similar Raman spectra and reducing I_D/I_G ratio also were observed in the wood-based chars [50,52], anthracene-based cokes [45] and cellulose-based carbon [39], which were synthesized at various HTTs.

Fig. 2 shows the FESEM micrographs of Si_3N_4 ceramic and its composites with different carbon contents and HTTs. In the porous Si_3N_4 ceramic (Fig. 2a and b), a typically interlocked microstructure that the rod-like β-Si_3N_4 grains connect randomly with each other is clearly observed. There are large number of three-dimensional network pores among the elongated β-Si_3N_4 grains, benefiting the impregnation process. Nevertheless, this intercrossing microstructure becomes blurred as the carbon is incorporated into the ceramic matrixes. It is because the carbon layer spreads out on the β-Si_3N_4 grains, and some pyrolytic carbon attach to the junction connecting grains. Interestingly, some ultrathin carbon films located in the pores also are detected. As the HTT and carbon content increases, the carbon film becomes more obvious. In addition, the EDX analysis (Fig. S3) demonstrates that amorphous carbon uniformly distributed in the composites.

Fig. 3A shows the pore size distributions of the porous Si_3N_4 ceramic and its composites at the HTT of 850 °C. The samples exhibit a single peak in the pore size distribution and their pore size is in the range from 200 to 600 nm. When the pyrolytic carbon was embedded into the porous ceramics, the median pore diameter of the composites becomes smaller. Fig. 3B shows the open porosity of the Si_3N_4 ceramic and its composites. It is found that the porosity of composites decreases with the increase of carbon content. This is because that more pyrolytic carbon occupies the pores of porous matrix.

3.2. Electrical property of the C/Si_3N_4 composites at different HTTs

Fig. 4A shows the ac conductivity (σ_{ac}) as a function of frequency for C/Si_3N_4 composites at different HTTs. The σ_{ac} of the composite at the HTT of 500 °C increases almost linearly with increasing frequency, showing a typical insulating behavior [53]. When the HTT

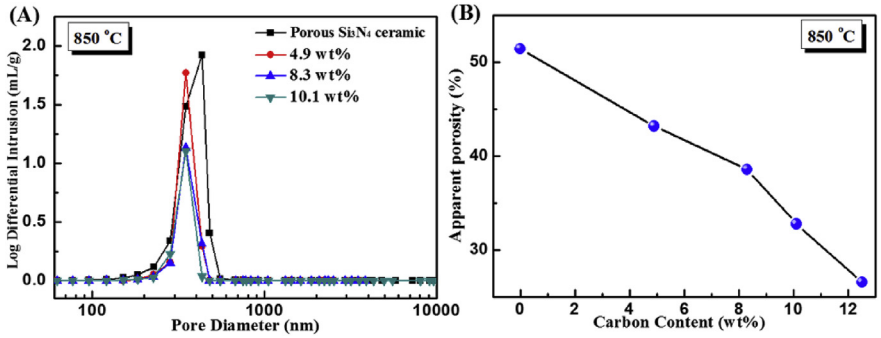

Fig. 3. Pore size distribution (A) and open porosity (B) of the Si_3N_4 ceramic and its composites with various carbon contents at the carbonizing temperature of 850 °C. (A colour version of this figure can be viewed online.)

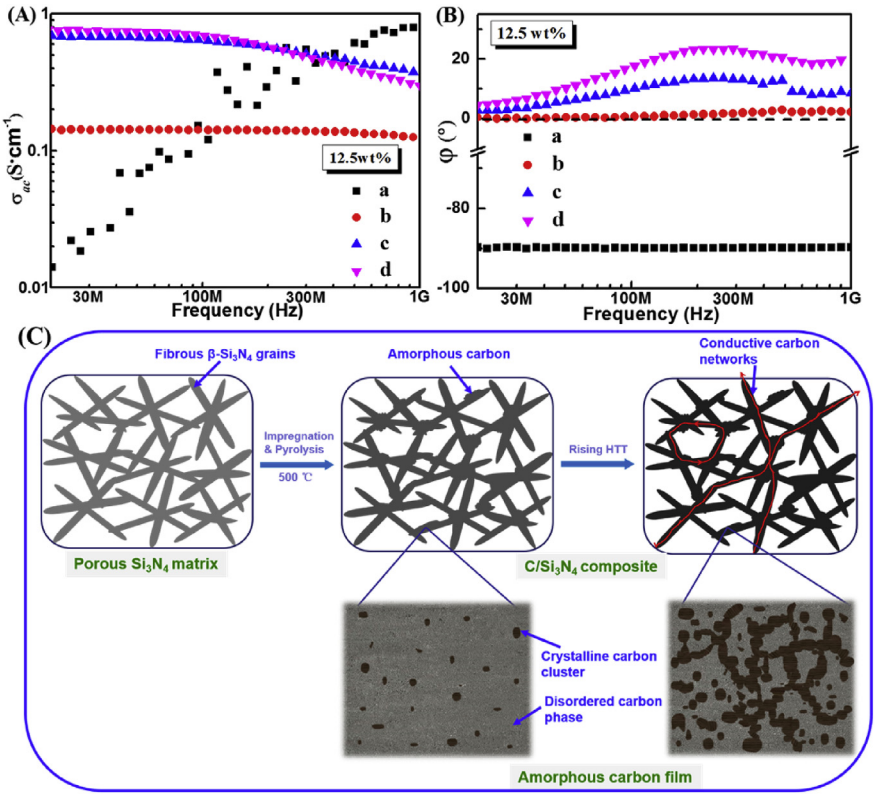

Fig. 4. Frequency dependences of electrical conductivity (A) and phase shift angle (B) for C/Si_3N_4 composites with 12.5 wt% carbon content at the carbonizing temperature of (a) 500, (b) 850, (c) 1100 and (d) 1300 °C. Schematic illustration of microstructural evolution (C) for the composites with rising carbonizing temperature. (A colour version of this figure can be viewed online.)

exceeds 500 °C, the composites exhibit a metal-like conductive behavior, and their σ_{ac} are frequency independent at low frequencies and then decreases as the frequency increases [20]. This conductive behavior should be attributed to the skin effect, which is a tendency for alternating current to flow mostly at the "skin" of an electrical conductor [54]. The skin depth (δ) can be expressed as eqn (5) [20,55].

$$\delta = \sqrt{\frac{2\rho}{\omega\mu}} \tag{5}$$

where ω ($\omega = 2\pi f$) is the angular frequency, ρ is resistivity and μ is the static permeability. The ρ and μ are constant for a given material, so the δ is inversely proportional to the square root of f. The increasing frequency will reduce the δ, and skin effect becomes more evident, leading to the decrease of σ_{ac} for composites, especially at high frequencies [20]. The occurrence of metal-like conductive behavior indicates carbon networks are formed in the composites. The conductive loops are not yet formed in carbon networks at low HTT (500 °C) due to the poor conductivity of amorphous carbon, while the conducting passway is formed in carbon networks at higher HTTs. In order to better understand the effect of HTT on conductive behavior, a schematic of microstructural evolution for the composites with rising HTT is shown in Fig. 4C. The pyrolytic carbon lays over the fibrous grains and locates in the pores. The amorphous carbon can be considered to compose of the highly conductive clusters (crystalline sp^2 carbon) embedded in a disordered matrix (amorphous sp^3 and sp^2 carbon) [39,56]. At the HTT of 500 °C, amorphous carbon is almost insulated with a small number of conducting carbon clusters. As the HTT elevates, the concentration of crystalline cluster increases due to the continuous growth of crystalline carbon and overall volumetric shrinkage, and thereby conductive clusters connect with each other, leading to the rapid increase in electrical conductivity of the amorphous carbon [57]. Hence the conducting networks are formed in the composites as rising HTT, along with a change of conductive behavior.

Fig. 4B represents frequency dependences of phase shift angle ($\varphi = \arctan(Z''/Z')$) for composites at various HTTs. Material, which is placed into an external ac electric field, can be regarded as a circuit consisting of capacitors (C), resistors (R) and/or inductors (L) [58]. In a circuit with only resistors, the voltage is in sync with current ($\varphi = 0°$). When capacitors or inductors are involved in the circuit, the current and voltage is not in phase [22,59]. Specifically, the phase between the current through a capacitor and the voltage across a capacitor is that the voltage lags current by 90° ($\varphi = -90°$). The relationship between the current and voltage through an inductor is that the voltage leads current by 90° ($\varphi = 90°$). In our obtained composites, the φ shifts from negative to positive on HTT increasing, indicating the occurrence of capacitive-inductive transition [60]. The φ values of the composite at 500 °C are observed in the range $-90° < \varphi < 0°$. This means that voltage phase falls behind the current phase, and capacitors play a dominant role in the circuit, so the composite manifests a capacitive character. Correspondingly, the composites with the elevated HTTs (≥850 °C) show an inductive behavior, as their φ values are in the range of 0–90°. The higher HTT results in the increase of conductivity in amorphous carbon, and many conductive loops are formed in the carbon networks of composites under high frequency electric field (Fig. 4C), so inductors dominate the equivalent circuit. Note that the φ of composite at 500 °C approaches −90°, which signifies that a circuit nearly just contains capacitors and resistors, showing a purely

capacitive response.

Frequency dependences of permittivity ($\varepsilon^* = \varepsilon' - j\varepsilon''$) for composites with various HTTs are given in Fig. 5. Substantial variation is observed in the dielectric curves of composites. Real part of permittivity (ε') of composite at 500 °C is positive and almost independent of frequency, while negative ε' is observed in the composites at high HTTs (≥850 °C), Fig. 5A. The negative ε' behavior is attributed to the low-frequency plasmon of free electrons in conductive carbon networks [23]. In our obtained carbon composites, there are lots of free carriers, providing the plasmonic state (Fig. 5C). When the frequency of external electric field is lower than the plasma frequency of free electrons, the negative ε' can be obtained [14,20]. The frequency dispersion of ε' can be described by the Drude model [14,61].

$$\varepsilon' = 1 - \frac{\omega_p^2}{\omega^2 + \Gamma_D^2} \tag{6}$$

$$\omega_P = \sqrt{\frac{n_{\text{eff}} e^2}{m_{\text{eff}} \varepsilon_0}} \tag{7}$$

where ω_p ($\omega_p = 2\pi f_p$) is the effective angular plasma frequency, Γ_D is damping parameter, n_{eff} is the effective concentration of free carriers, m_{eff} is the effective mass of the carriers, e is the electron charge (1.6×10^{-19} C) and ε_0 is the permittivity of free space (8.85×10^{-12} F/m). The fitting curves (solid line), which are obtained using OriginPro 8 software according to eqn (6), are in good agreement with the experimental data of ε' (dotted line). The fitting values of ω_p for composites with rising HTT are 9.44, 55.81 and 65.62 GHz, respectively. From eqn (7), the ω_p is found to depend on the n_{eff} and m_{eff}. In the obtained composites, the increasing HTT bring about more free carriers in carbon networks, leads to the elevated n_{eff} and reduced m_{eff} [20]. Thus, the ω_p moves toward a higher frequency on increasing HTT. The magnitude of negative ε' also becomes larger with rising the HTT, which is due to the larger ω_p (according to eqn (6)). It is notable that the negative magnitude of ε' for composite at 850 °C is small ranging from −50 to −10 in the testing frequency. Table 1 shows the comparison of the negative ε' in various random metamaterials. In those metamaterials with metal or carbon nano-materials, the negative magnitude of ε' generally was enormous at the frequency lower than their plasma frequency, which obstructs many applications of the metamaterials. In our work, the weakly negative ε' behavior with low frequency dispersion is achieved in the amorphous carbon composites, which arises from the moderate carrier concentration of the conductive carbon network [30,62]. The obtained small and stable negative ε' makes a possibility for their applications in the capacitor, microwave absorbers, antenna and sensor [30–32,63–66].

The imaginary part of permittivity (ε'') is signal of dielectric loss, which mainly includes the conduction loss (ε_c'') and relaxation loss (ε_r'') [70]. According to Debye theory, the ε'' can be described as the following [71,72].

$$\varepsilon'' = \varepsilon_c'' + \varepsilon_r'' \tag{8}$$

$$\varepsilon_c'' = \frac{\sigma_{dc}}{\omega \varepsilon_0} \tag{9}$$

$$\varepsilon_r'' = \frac{\varepsilon_S - \varepsilon_\infty}{1 + \omega^2 \tau^2} \omega\tau \tag{10}$$

where σ_{dc} is the direct current conductivity, ε_s is the static permittivity, ε_∞ is the high-frequency limit permittivity and τ is relaxation time. The conduction loss of composites stems from the electric leakage among carbon membranes. The relaxation loss mainly arises from the defect dipole and interfacial polarization processes [71]. The defect dipoles originate from the charge unbalance in the amorphous carbon. The interfacial polarization is also generated from the charge unbalance, which exists at the C–Si_3N_4 interfaces. For the composite at 500 °C, the ε'' is small (no more than 0.1) in the testing frequency (Fig. 5B), and is primarily dominated by relaxation loss, while the low conduction loss can be ignored [70,73]. As the HTT reaches 850 °C, the ε'' jumps to a high value (~10^3), which is the inevitable consequence of the formation

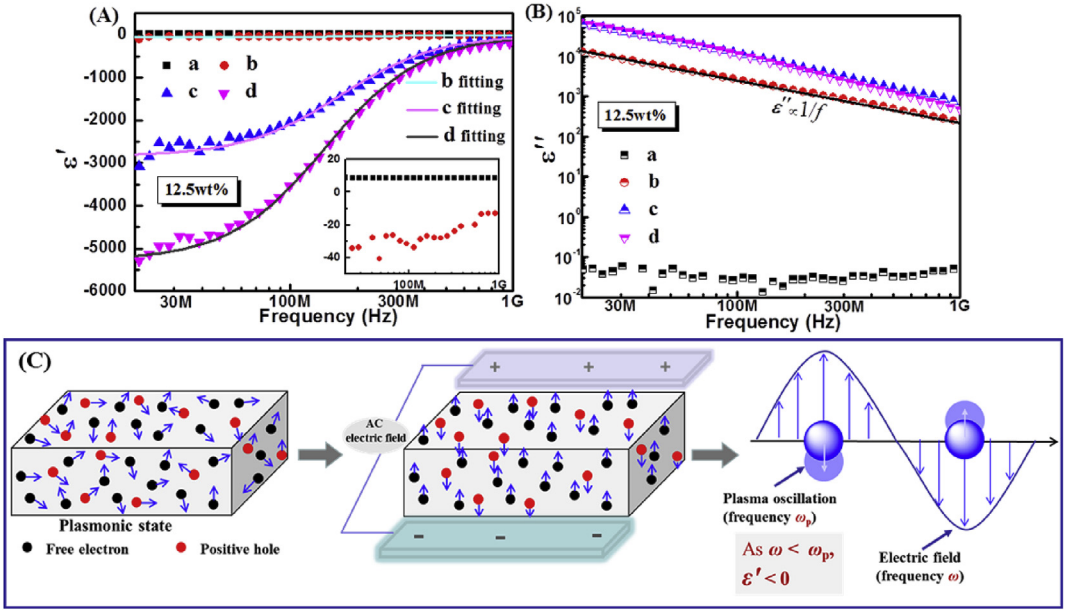

Fig. 5. Frequency dependences of permittivity (A, B) for C/Si_3N_4 composites with 12.5 wt% carbon content at the carbonizing temperature of (a) 500, (b) 850, (c) 1100 and (d) 1300 °C. Schematic diagram for generating mechanism (C) of negative permittivity behavior. (A colour version of this figure can be viewed online.)

Table 1
The comparison of the negative permittivity in various random metamaterials.

Material system	Filler content	ω_p/GHz	Magnitude of negative ε'	Testing frequency band	Refs.
Iron-alumina	27 wt%	1306	~-10^6	30 MHz–1GHz	[20]
Nickel-alumina	35 wt%	167	~-10^5	10 MHz–1GHz	[14]
Copper-polyphenylene Sulfide resin	16.4 vol%	–	~-10^4	10 MHz–10 GHz	[23]
Nickel chain-poly(vinylidene fluoride)	6 wt%	–	~-10^4	100 Hz–100 kHz	[67]
Silver-alumina	41 wt%	101	~-10^4	100 MHz–1GHz	[68]
FeNiMo-alumina	30 wt%	56.5	~-10^5	10 MHz–1GHz	[26]
Carbon nanotube-polypropylene	2 wt%	–	~-10^4	100 Hz–1MHz	[69]
Graphene-polyaniline	3 wt%	–	~-10^4	20 Hz–1MHz	[29]
Carbon nanofiber- polypyrrole	5 wt%	–	~-10^3	20 Hz–1MHz	[28]
Pyrolytic carbon-silicon nitride	12.5 wt% (850 °C)	9.44	~−50	20 MHz–1GHz	This work

of conductive networks in the composite [74]. The enhanced conductivity leads to a rapid increase of conduction loss. The composites with the high HTTs show an inverse linear correlation between ε'' and frequency, which accords with eqn (9) [72,75]. Thus, we believe that the conduction loss plays a dominant role in the dielectric loss ($\varepsilon'' \approx \varepsilon_c''$).

3.3. Electrical property of the C/Si_3N_4 composites with different carbon contents

Apart from the HTT, the carbon content also exerts a great influence on the electrical property of the C/Si_3N_4 composites. Thus, a series of composites with carbon contents of 4.9, 8.3 and 10.1 wt% were further prepared, respectively. Fig. 6 exhibits the frequency dependences of σ_{ac} for the composites with various carbon contents. The rising carbon content and HTT lead to the increase of the σ_{ac} due to the formative more carbon networks for facilitating free carrier transfer. Two different dispersion behaviors of σ_{ac} are observed in these composites. The composites at the HTT of 850 °C show a frequency independent conductivity in the low frequency region and then exhibit a clearly increasing trend of σ_{ac} at the high frequencies. The σ_{ac} depending on frequency follows an empirical power law given as [20,58].

$$\sigma_{ac} = \sigma_{dc} + A\omega^n \tag{11}$$

where A is the pre-exponential factor and n is the fractional exponent. The good simulated results indicate that a hopping conduction behavior appears in the composites [20,30]. The other composites show a metal-like conductive behavior, and the σ_{ac} decreases with increasing frequency due to the skin effect [58]. Besides, the composites with 4.9 wt% carbon content undergo a change of conductive mechanism as the HTT elevates (Fig. 6A). This result manifests the carbon networks are formed in the composites

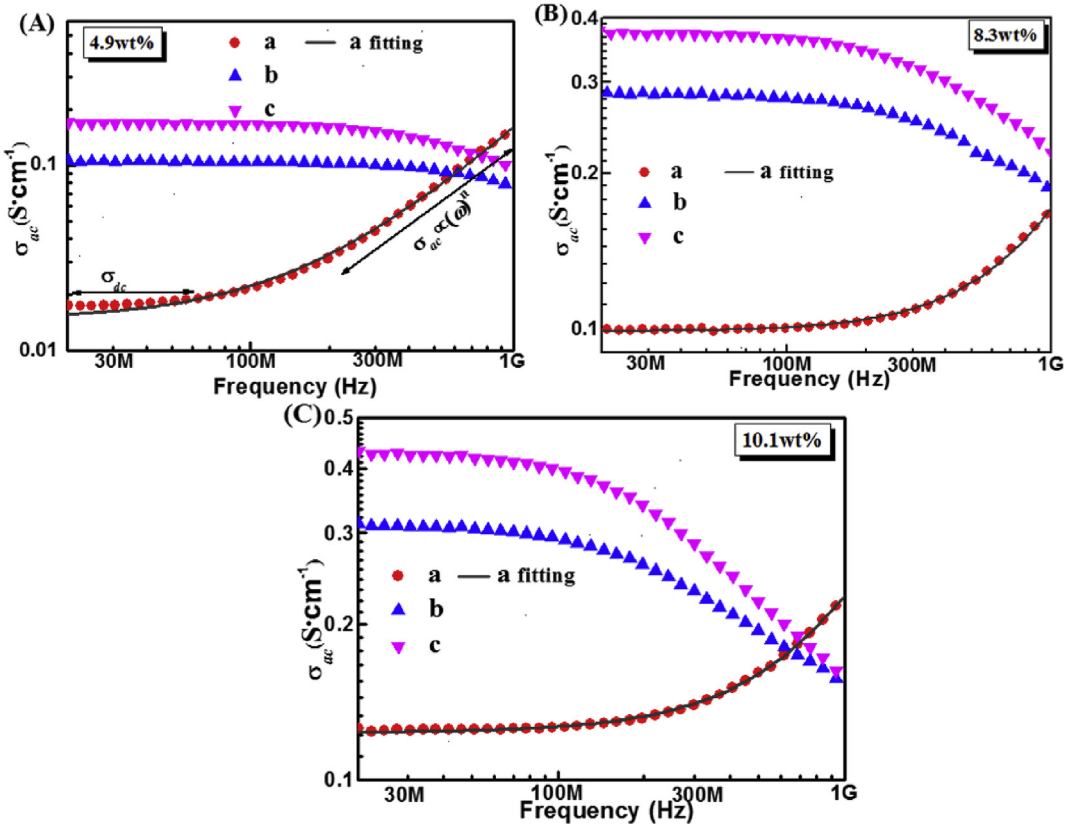

Fig. 6. Frequency dependences of σ_{ac} for the C/Si_3N_4 composites with various carbon contents at the carbonizing temperature of (a) 850, (b) 1100 and (c) 1300 °C. (A colour version of this figure can be viewed online.)

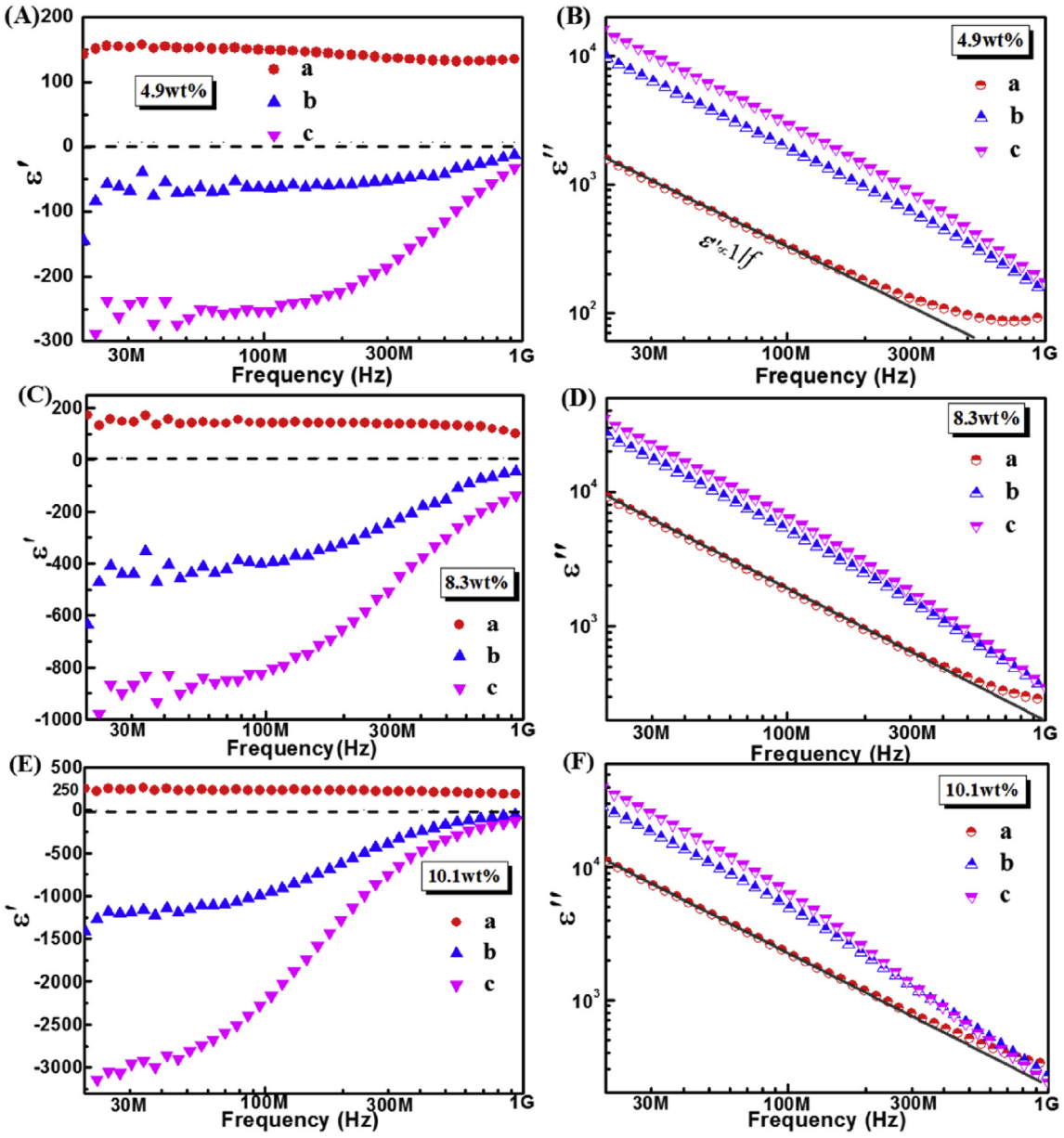

Fig. 7. Frequency dependences of permittivity for the C/Si_3N_4 composites with various carbon contents at the carbonizing temperature of (a) 850, (b) 1100 and (c) 1300 °C. (A colour version of this figure can be viewed online.)

even at the low carbon content; nevertheless, the conductive loops are not formed in carbon networks at 850 °C, owing to the weak conductivity of amorphous carbon.

Fig. 7 presents the frequency dependences of permittivity for the composites with different carbon contents. The negative ε' was also observed when the carbon contents are reduced to 4.9, 8.3 and 10.1 wt%, Fig. 7A, C and E. Lower carbon content and lower HTT could reduce carrier concentration, leading to the decrease of the negative ε' amplitude as described by the Drude model [31]. That is, the values of negative ε' could be effectively adjusted by the carbon content and HTT. For the composites at 850 °C, the low-intensity free carrier in the carbon networks is insufficient for the appearance of negative ε' in the measured frequency band [20]. Their positive ε' become larger with increasing carbon content due to enlarged C–Si_3N_4 interface areas [24]. Furthermore, an inductive behavior ($Z''>0$) also is observed in the composites along with the negative ε' (Fig. S4). Similar results were obtained in many other random metamaterials containing carbon or metal component [20–22,24,30]. Hence, we believe that the inductive behavior is a characteristic of negative ε' phenomenon [54]. The frequency dispersions of ε'' for the composites were illustrated in Fig. 7B, D and F. The larger ε'' values are observed in the composites with the higher carbon content and HTT, causing by the enhanced conduction loss. As discussed above, if the conduction loss governs dissipative processes, the plots of ε'' versus f will show a linear decrease relation in a logarithmic scale ($\varepsilon'' \propto f^{-1}$) [75]. Whereas, for the composites at 850 °C, the curves of ε'' deviate from the linear relationship at the high frequency reign, which implies that the dominant role in the dielectric loss changes from the conduction loss to the polarization loss as the frequency increases. This result can be explained by the reason that the increase of frequency leads to the smaller conduction loss (according to eqn (9)), and the

polarization loss makes a primary contribution to the dielectric loss at the high frequencies.

4. Conclusion

In this paper, the C/Si_3N_4 composites consisting of amorphous carbon hosted in porous Si_3N_4 were prepared by an infiltration-pyrolysis process. A tunable and weakly negative permittivity behavior has been evidenced in the composites with different HTTs and carbon contents. The obtained negative permittivity behavior was attributed to the low frequency plasmonic state derived from the formative conducting carbon networks. The negative value of permittivity could be effectively adjusted by controlling the HTT and carbon content. Small magnitude of negative permittivity in the tested frequency was observed ranging from −50 to −10, which arisen from the lower carrier density of the conductive carbon networks in the composite. And the Drude model was given a good description of the dielectric response. This study can potentially be used to develop the random metamaterials with tunable negative permittivity for various practical applications, such as capacitor, electromagnetic absorption and shielding.

Acknowledgements

The authors are grateful for the financial support from the National Basic Research Program of China (973 Program, No. 2014CB643306), National Natural Science Foundation of China (No. 51601105, 51402170, 51602194 and 51602195), and the Natural Science Foundation of Shandong Province (No. ZR2016EMM09). C. Cheng acknowledges the support from the program for outstanding PhD candidate of Shandong University and the China Scholarship Council.

Appendix A. Supplementary data

Supplementary data related to this article can be found at http://dx.doi.org/10.1016/j.carbon.2017.09.037.

References

[1] D.R. Smith, J.B. Pendry, M.C. Wiltshire, Metamaterials and negative refractive index, Science 305 (5685) (2004) 788–792.
[2] H. Da, X. Yan, Metamaterials in multilayer graphene photonics: control of negative refraction, Carbon 100 (2016) 74–80.
[3] P. Richner, H. Eghlidi, S.J. Kress, M. Schmid, D.J. Norris, D. Poulikakos, Printable nanoscopic metamaterial absorbers and images with diffraction-limited resolution, ACS Appl. Mater. Interfaces 8 (18) (2016) 11690–11697.
[4] W. Fan, B. Yan, Z. Wang, L. Wu, Three-dimensional all-dielectric metamaterial solid immersion lens for subwavelength imaging at visible frequencies, Sci. Adv. 2 (8) (2016), e1600901.
[5] R. Liu, C. Ji, J. Mock, J. Chin, T. Cui, D. Smith, Broadband ground-plane cloak, Science 323 (5912) (2009) 366–369.
[6] D. Schurig, J. Mock, B. Justice, S.A. Cummer, J.B. Pendry, A. Starr, D. Smith, Metamaterial electromagnetic cloak at microwave frequencies, Science 314 (5801) (2006) 977–980.
[7] C.M. Watts, X. Liu, W.J. Padilla, Metamaterial electromagnetic wave absorbers, Adv. Mater. 24 (23) (2012).
[8] A. Moreau, C. Ciraci, J.J. Mock, R.T. Hill, Q. Wang, B.J. Wiley, A. Chilkoti, D.R. Smith, Controlled-reflectance surfaces with film-coupled colloidal nanoantennas, Nature 492 (7427) (2012) 86–89.
[9] N. Yi, Z. Liu, S. Sun, Q. Song, S. Xiao, Mid-infrared tunable magnetic response in graphene-based diabolo nanoantennas, Carbon 94 (2015) 501–506.
[10] K.V. Sreekanth, Y. Alapan, M. ElKabbash, E. Ilker, M. Hinczewski, U.A. Gurkan, A. De Luca, G. Strangi, Extreme sensitivity biosensing platform based on hyperbolic metamaterials, Nat. Mater. (2016) 621–627.
[11] J. Fang, I. Levchenko, W. Yan, I. Aharonovich, M. Aramesh, S. Prawer, K.K. Ostrikov, Plasmonic metamaterial sensor with ultra-high sensitivity in the visible spectral range, Adv. Opt. Mater. 3 (6) (2015) 750–755.
[12] S. Jahani, Z. Jacob, All-dielectric metamaterials, Nat. Nanotechnol. 11 (1) (2016) 23–36.
[13] N.I. Zheludev, The road ahead for metamaterials, Science 328 (5978) (2010) 582–583.
[14] Z. Shi, R. Fan, Z. Zhang, L. Qian, M. Gao, M. Zhang, L. Zheng, X. Zhang, L. Yin, Random composites of nickel networks supported by porous alumina toward double negative materials, Adv. Mater. 24 (17) (2012) 2349–2352.
[15] H. Chen, Metamaterials: constitutive parameters, performance, and chemical methods for realization, J. Mater. Chem. 21 (18) (2011) 6452–6463.
[16] Y. Huang, Z. Yao, F. Hu, C. Liu, L. Yu, Y. Jin, X. Xu, Tunable circular polarization conversion and asymmetric transmission of planar chiral graphene-metamaterial in terahertz region, Carbon 119 (2017) 305–313.
[17] J. Gao, X. Wu, Q. Li, S. Du, F. Huang, L. Liang, H. Zhang, F. Zhuge, H. Cao, Y. Song, Template-free growth of well-ordered silver nano forest/ceramic metamaterial films with tunable optical responses, Adv. Mater. 29 (2017), 1605324.
[18] B. Li, G. Sui, W.H. Zhong, Single negative metamaterials in unstructured polymer nanocomposites toward selectable and controllable negative permittivity, Adv. Mater. 21 (41) (2009) 4176–4180.
[19] C. Cheng, R. Fan, Y. Ren, T. Ding, L. Qian, J. Guo, X. Li, L. An, Y. Lei, Y. Yin, Radio frequency negative permittivity in random carbon nanotubes/alumina nanocomposites, Nanoscale 9 (18) (2017) 5779–5787.
[20] Z. Shi, R. Fan, K. Yan, K. Sun, M. Zhang, C. Wang, X. Liu, X. Zhang, Preparation of iron networks hosted in porous alumina with tunable negative permittivity and permeability, Adv. Funct. Mater. 23 (33) (2013) 4123–4132.
[21] K. Sun, R. Fan, Y. Yin, J. Guo, X.F. Li, Y. Lei, L. An, C. Cheng, Z. Guo, Tunable negative permittivity with Fano-like resonance and magnetic property in percolative silver/yittrium iron garnet nanocomposites, J. Phys. Chem. C 121 (2017) 7564–7571.
[22] Z. Shi, R. Fan, Z. Zhang, K. Yan, X. Zhang, K. Sun, X. Liu, C. Wang, Experimental realization of simultaneous negative permittivity and permeability in Ag/$Y_3Fe_5O_{12}$ random composites, J. Mater. Chem.C 1 (8) (2013) 1633–1637.
[23] T. Tsutaoka, T. Kasagi, S. Yamamoto, K. Hatakeyama, Low frequency plasmonic state and negative permittivity spectra of coagulated Cu granular composite materials in the percolation threshold, Appl. Phys. Lett. 102 (18) (2013), 181904.
[24] X. Wang, Z. Shi, M. Chen, R. Fan, K. Yan, K. Sun, S. Pan, M. Yu, Tunable electromagnetic properties in Co/Al_2O_3 cermets prepared by wet chemical method, J. Am. Ceram. Soc. 97 (10) (2014) 3223–3229.
[25] M. Chen, R. Fan, M. Gao, S. Pan, M. Yu, Z. Zhang, Negative permittivity behavior in $Fe_{50}Ni_{50}$/Al_2O_3 magnetic composite near percolation threshold, J. Magn. Magn. Mater. 381 (2015) 105–108.
[26] M. Chen, M. Gao, F. Dang, N. Wang, B. Zhang, S. Pan, Tunable negative permittivity and permeability in FeNiMo/Al_2O_3 composites prepared by hot-pressing sintering, Ceram. Int. 42 (5) (2016) 6444–6449.
[27] Q. Hou, K. Yan, R. Fan, Z. Zhang, M. Chen, K. Sun, C. Cheng, Experimental realization of tunable negative permittivity in percolative $Fe_{78}Si_9B_{13}$/epoxy composites, RSC Adv. 5 (13) (2015) 9472–9475.
[28] J. Zhu, X. Zhang, N. Haldolaarachchige, Q. Wang, Z. Luo, J. Ryu, D.P. Young, S. Wei, Z. Guo, Polypyrrole metacomposites with different carbon nanostructures, J. Mater. Chem. 22 (11) (2012) 4996–5005.
[29] J. Zhu, H. Gu, Z. Luo, N. Haldolaarachige, D.P. Young, S. Wei, Z. Guo, Carbon nanostructure-derived polyaniline metacomposites: electrical, dielectric, and giant magnetoresistive properties, Langmuir 28 (27) (2012) 10246–10255.
[30] R. Gholipur, Z. Khorshidi, A. Bahari, Enhanced absorption performance of carbon nanostructure based metamaterials and tuning impedance matching behavior by an external AC electric field, ACS Appl. Mater. Interfaces 9 (2017) 12528–12539.
[31] J. Wang, Z. Shi, F. Mao, S. Chen, X. Wang, Bilayer polymer metacomposites containing negative permittivity layer for new high-k materials, ACS Appl. Mater. Interfaces 9 (2017) 1793–1800.
[32] Z. Liu, X. Liu, S. Huang, P. Pan, J. Chen, G. Liu, G. Gu, Automatically acquired broadband plasmonic-metamaterial black absorber during the metallic film-formation, ACS Appl. Mater. Interfaces 7 (8) (2015) 4962–4968.
[33] Y. Wang, L. Wu, T.I. Wong, M. Bauch, Q. Zhang, J. Zhang, X. Liu, X. Zhou, P. Bai, J. Dostalek, Directional fluorescence emission co-enhanced by localized and propagating surface plasmons for biosensing, Nanoscale 8 (15) (2016) 8008–8016.
[34] C. Cheng, R. Fan, L. Qian, X. Wang, L. Dong, Y. Yin, Tunable negative permittivity behavior of random carbon/alumina composites in the radio frequency band, RSC Adv. 6 (90) (2016) 87153–87158.
[35] A. Boltasseva, H.A. Atwater, Low-loss plasmonic metamaterials, Science 331 (6015) (2011) 290–291.
[36] C. Cheng, K. Yan, R. Fan, L. Qian, Z. Zhang, K. Sun, M. Chen, Negative permittivity behavior in the carbon/silicon nitride composites prepared by impregnation-carbonization approach, Carbon 96 (2016) 678–684.
[37] M. Chen, X. Wang, Z. Zhang, K. Sun, C. Cheng, F. Dang, Negative permittivity behavior and magnetic properties of C/YIG composites at radio frequency, Mater. Des. 97 (2016) 454–458.
[38] S.R.P. Silva, Properties of Amorphous Carbon, 2003.
[39] Y.R. Rhim, D. Zhang, D.H. Fairbrother, K.A. Wepasnick, K.J. Livi, R.J. Bodnar, D.C. Nagle, Changes in electrical and microstructural properties of microcrystalline cellulose as function of carbonization temperature, Carbon 48 (4) (2010) 1012–1024.
[40] N. Dwivedi, R.J. Yeo, Z. Zhang, C. Dhand, S. Tripathy, C.S. Bhatia, Direct observation of thickness and foreign interlayer driven abrupt structural transformation in ultrathin carbon and hybrid silicon nitride/carbon films, Carbon 115 (2017) 701–719.
[41] W. Zhu, S. Ge, Q. Shao, Adsorption properties of ZrO_2 hollow microboxes

prepared using $CaCO_3$ cubes as templates, RSC Adv. 6 (85) (2016) 81736–81743.
[42] M. Xie, J. Yang, J. Liang, X. Guo, W. Ding, In situ hydrothermal deposition as an efficient catalyst supporting method towards low-temperature graphitization of amorphous carbon, Carbon 77 (2014) 215–225.
[43] A. Szczurek, A. Ortona, L. Ferrari, E. Rezaei, G. Medjahdi, V. Fierro, D. Bychanok, P. Kuzhir, A. Celzard, Carbon periodic cellular architectures, Carbon 88 (2015) 70–85.
[44] T. Wu, Q. Shao, S. Ge, L. Bao, Q. Liu, The facile preparation of novel magnetic zirconia composites with the aid of carboxymethyl chitosan and their efficient removal of dye, RSC Adv. 6 (63) (2016) 58020–58027.
[45] S. Bernard, O. Beyssac, K. Benzerara, N. Findling, G. Tzvetkov, G. Brown, XANES, Raman and XRD study of anthracene-based cokes and saccharose-based chars submitted to high-temperature pyrolysis, Carbon 48 (9) (2010) 2506–2516.
[46] Y.R. Rhim, D. Zhang, M. Rooney, D.C. Nagle, D.H. Fairbrother, C. Herman, D.G. Drewry, Changes in the thermophysical properties of microcrystalline cellulose as function of carbonization temperature, Carbon 48 (1) (2010) 31–40.
[47] S.S. Tzeng, Y.G. Chr, Evolution of microstructure and properties of phenolic resin-based carbon/carbon composites during pyrolysis, Mater. Chem. Phys. 73 (2) (2002) 162–169.
[48] J. McDonald-Wharry, M. Manley-Harris, K. Pickering, Carbonisation of biomass-derived chars and the thermal reduction of a graphene oxide sample studied using Raman spectroscopy, Carbon 59 (2013) 383–405.
[49] Y. Cao, J. Huang, Y. Li, S. Qiu, J. Liu, A. Khasanov, M.A. Khan, D.P. Young, F. Peng, D. Cao, One-pot melamine derived nitrogen doped magnetic carbon nano-adsorbents with enhanced chromium removal, Carbon 109 (2016) 640–649.
[50] D. Deldicque, J.N. Rouzaud, B. Velde, A Raman-HRTEM study of the carbonization of wood: a new Raman-based paleothermometer dedicated to archaeometry, Carbon 102 (2016) 319–329.
[51] A.C. Ferrari, J. Robertson, Interpretation of Raman spectra of disordered and amorphous carbon, Phys. Rev. B 61 (20) (2000) 14095.
[52] O. Paris, C. Zollfrank, G.A. Zickler, Decomposition and carbonisation of wood biopolymers-a microstructural study of softwood pyrolysis, Carbon 43 (1) (2005) 53–66.
[53] K. Shehzad, Z.M. Dang, M.N. Ahmad, R.U.R. Sagar, S. Butt, M.U. Farooq, T.B. Wang, Effects of carbon nanotubes aspect ratio on the qualitative and quantitative aspects of frequency response of electrical conductivity and dielectric permittivity in the carbon nanotube/polymer composites, Carbon 54 (2013) 105–112.
[54] K. Yan, R. Fan, Z. Shi, M. Chen, L. Qian, Y. Wei, K. Sun, J. Li, Negative permittivity behavior and magnetic performance of perovskite $La_{1-x}Sr_xMnO_3$ at high-frequency, J. Mater. Chem. C 2 (6) (2014) 1028–1033.
[55] X. Liu, X. Yin, L. Kong, Q. Li, Y. Liu, W. Duan, L. Zhang, L. Cheng, Fabrication and electromagnetic interference shielding effectiveness of carbon nanotube reinforced carbon fiber/pyrolytic carbon composites, Carbon 68 (2014) 501–510.
[56] A.K. Kercher, D.C. Nagle, Microstructural evolution during charcoal carbonization by X-ray diffraction analysis, Carbon 41 (1) (2003) 15–27.
[57] H. Sugimoto, M. Norimoto, Dielectric relaxation due to interfacial polarization for heat-treated wood, Carbon 42 (1) (2004) 211–218.
[58] Z. Shi, S. Chen, K. Sun, X. Wang, R. Fan, X. Wang, Tunable radio-frequency negative permittivity in nickel-alumina “natural” meta-composites, Appl. Phys. Lett. 104 (25) (2014), 252908.
[59] T. Koltunowicz, P. Zhukowski, V. Bondariev, A. Saad, J. Fedotova, A. Fedotov, M. Milosavljević, J. Kasiuk, Enhancement of negative capacitance effect in $(CoFeZr)_x(CaF_2)_{(100-x)}$ nanocomposite films deposited by ion beam sputtering in argon and oxygen atmosphere, J. Alloys. Compd. 615 (2014) S361–S365.
[60] P. Zukowski, T.N. Koltunowicz, V. Bondariev, A.K. Fedotov, J.A. Fedotova, Determining the percolation threshold for $(FeCoZr)_x(CaF_2)_{(100-x)}$ nanocomposites produced by pure argon ion-beam sputtering, J. Alloys. Compd. 683 (2016) 62–66.
[61] J. Pendry, A. Holden, W. Stewart, I. Youngs, Extremely low frequency plasmons in metallic mesostructures, Phys. Rev. Lett. 76 (25) (1996) 4773.
[62] K. Sun, P. Xie, Z. Wang, T. Su, Q. Shao, J. Ryu, X. Zhang, J. Guo, A. Shankar, J. Li, Flexible polydimethylsiloxane/multi-walled carbon nanotubes membranous metacomposites with negative permittivity, Polymer 125 (2017) 50–57.
[63] X. Yin, L. Kong, L. Zhang, L. Cheng, N. Travitzky, P. Greil, Electromagnetic properties of Si-C-N based ceramics and composites, Int. Mater. Rev. 59 (6) (2014) 326–355.
[64] Q. Yuchang, W. Qinlong, L. Fa, Z. Wancheng, Temperature dependence of the electromagnetic properties of graphene nanosheet reinforced alumina ceramics in the X-band, J. Mater. Chem. C 4 (22) (2016) 4853–4862.
[65] H. Jin, Q. Chen, Z. Chen, Y. Hu, J. Zhang, Multi-LeapMotion sensor based demonstration for robotic refine tabletop object manipulation task, CAAI Trans. Intell. Technol. 1 (1) (2016) 104–113.
[66] X. Zhang, H. Gao, M. Guo, G. Li, Y. Liu, D. Li, A study on key technologies of unmanned driving, CAAI Trans. Intell. Technol. 1 (1) (2016) 4–13.
[67] B. Zhao, C.B. Park, Tunable electromagnetic shielding properties of conductive poly (vinylidene fluoride)/Ni chain composite films with negative permittivity, J. Mater. Chem. C 5 (28) (2017) 6954–6961.
[68] Z. Shi, R. Fan, Z. Zhang, H. Gong, J. Ouyang, Y. Bai, X. Zhang, L. Yin, Experimental and theoretical investigation on the high frequency dielectric properties of Ag/Al_2O_3 composites, Appl. Phys. Lett. 99 (3) (2011), 032903.
[69] X. Zhang, X. Yan, Q. He, H. Wei, J. Long, J. Guo, H. Gu, J. Yu, J. Liu, D. Ding, Electrically conductive polypropylene nanocomposites with negative permittivity at low carbon nanotube loading levels, ACS Appl. Mater. Interfaces 7 (11) (2015) 6125–6138.
[70] J. Chang, G. Liang, A. Gu, S. Cai, L. Yuan, The production of carbon nanotube/epoxy composites with a very high dielectric constant and low dielectric loss by microwave curing, Carbon 50 (2) (2012) 689–698.
[71] X. Liu, L.S. Wang, Y. Ma, H. Zheng, L. Lin, Q. Zhang, Y. Chen, Y. Qiu, D.L. Peng, Enhanced microwave absorption properties by tuning cation deficiency of perovskite oxides of two-dimensional $LaFeO_3$/C composite in X-Band, ACS Appl. Mater. Interfaces 9 (8) (2017) 7601–7610.
[72] B. Wang, G. Liang, Y. Jiao, A. Gu, L. Liu, L. Yuan, W. Zhang, Two-layer materials of polyethylene and a carbon nanotube/cyanate ester composite with high dielectric constant and extremely low dielectric loss, Carbon 54 (2013) 224–233.
[73] Z. Sun, L. Zhang, F. Dang, Y. Liu, Z. Fei, Q. Shao, H. Lin, J. Guo, L. Xiang, N. Yerra, Experimental and simulation understanding of morphology controlled barium titanate nanoparticles under co-adsorption of surfactants, CrystEngComm 19 (2017) 3288–3298.
[74] A. Ameli, M. Arjmand, P. Pötschke, B. Krause, U. Sundararaj, Effects of synthesis catalyst and temperature on broadband dielectric properties of nitrogen-doped carbon nanotube/polyvinylidene fluoride nanocomposites, Carbon 106 (2016) 260–278.
[75] G. Zheng, X. Yin, S. Liu, X. Liu, J. Deng, Q. Li, Improved electromagnetic absorbing properties of Si_3N_4-SiC/SiO_2 composite ceramics with multi-shell microstructure, J. Eur. Ceram. Soc. 33 (11) (2013) 2173–2180.